**THE EUROPEAN
PHYSICAL JOURNAL C**

CrossMark

Effects of local features of the inflaton potential on the spectrum and bispectrum of primordial perturbations

Alexander Gallego Cadavid[1,3], **Antonio Enea Romano**[1,2,3,4,5,a], **Stefano Gariazzo**[4,5]

[1] Instituto de Fisica, Universidad de Antioquia, A.A.1226, Medellin, Colombia
[2] Department of Physics, University of Crete, 71003 Heraklion, Greece
[3] Yukawa Institute for Theoretical Physics, Kyoto University, Kyoto, Japan
[4] Department of Physics, University of Torino, Via P. Giuria 1, 10125 Torino, Italy
[5] INFN, Sezione di Torino, Via P. Giuria 1, 10125 Torino, Italy

Abstract We study the effects of a class of features of the potential of slow-roll inflationary models corresponding to a step symmetrically dumped by an even power negative exponential factor, which we call local features. Local-type features differ from other branch-type features considered previously, because the potential is only affected in a limited range of the scalar field value, and they are symmetric with respect to the location of the feature. This type of feature only affects the spectrum and bispectrum in a narrow range of scales which leave the horizon during the time interval corresponding to the modification of the potential. On the contrary branch-type features have effects on all the perturbation modes leaving the horizon when the field value is within the interval defining the branch, introducing for example differences in the power spectrum between large and small scale which are absent in the case of local-type features. The spectrum and bispectrum of primordial curvature perturbations are affected by oscillations around the scale k_0 exiting the horizon at the time τ_0 corresponding to the feature. We also compute the effects of the features on the CMB temperature and polarization spectra, showing the effects of different choices of parameters.

1 Introduction

Theoretical cosmology has entered in the last decades in a new era in which different models can be compared directly to high-precision observations [1–4]. One fundamental source of information as regards the early Universe is the cosmic microwave background (CMB) radiation, which according to the standard cosmological model consists of the photons

that decoupled from the primordial plasma when the neutral hydrogen atoms started to form.

According to the inflation theory [5,6] the CMB temperature anisotropies arose from primordial curvature perturbation, whose spectrum is approximately scale invariant. An approximately scale invariant spectrum of curvature perturbation, with a small tilt, provides a good fit of CMB data [4], but recent analyses of the WMAP and Planck data have shown evidence of a feature around the scale $k = 0.002\,\mathrm{Mpc}^{-1}$ in the power spectrum of primordial scalar fluctuations [7–23] that corresponds to a dip in the CMB temperature spectrum at $l \simeq 20$. This kind of feature of the curvature perturbations spectrum provides an important observational motivation to find theoretical models able to explain it. In particular in this paper we will consider the effects of features of the inflaton potential in single field inflationary model as possible explanation of the features of the power spectrum.

The effects of features of the inflaton potential were first studied by Starobinsky [24], and CMB data have shown some glitches of the power spectrum [25,26] compatible with these features [27–31].

The Starobinsky model and its generalizations [32–36] belong to a class of branch features (BFs) which involve a step function or a smoothed version of the latter [37], and consequently introduce a distinction between a left and right branch of the potential. In this paper instead we will consider the effects of local features (LF) [38] which only modify the potential locally in field space, while leaving it unaffected sufficiently far from the feature. The important consequence is that also the effects of LFs on the spectrum and bispectrum are local, while BFs modify the spectrum in a wider range of scales. Features of the inflaton potential could be produced by different sources [39,40], for example particle production
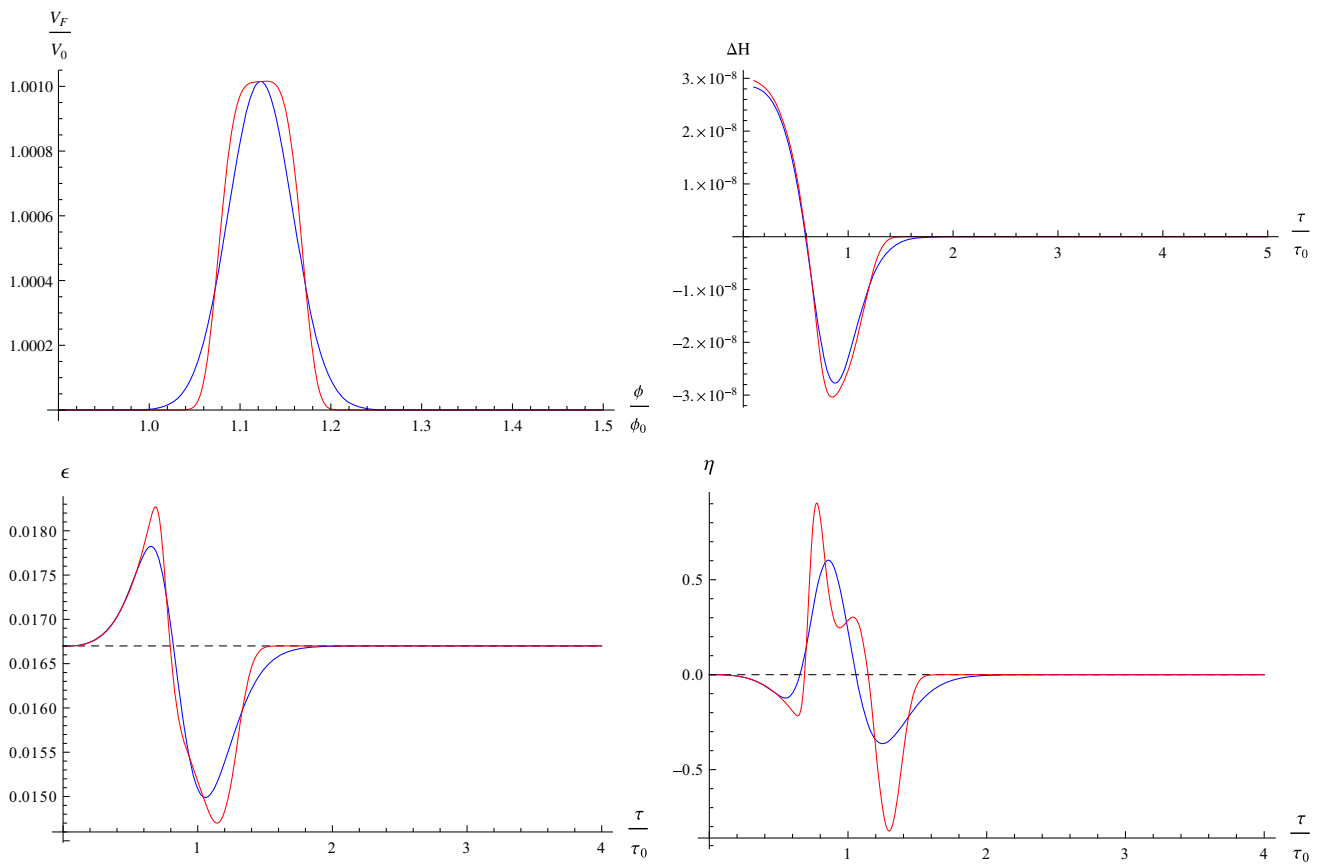
a e-mail: aer@physics.uoc.gr

Fig. 1 From *left to right* and *top to bottom* the numerically computed V_F/V_0, ΔH, ϵ, and η are plotted for $\lambda = 10^{-11}$, $\sigma = 0.05$, and $n = 1$ (*blue*) and $n = 2$ (*red*). The *dashed black lines* correspond to the featureless behavior

[41] or phase transitions [42], but here we will only study their effects adopting a phenomenological approach, as done originally by Starobinsky in his seminal work (Fig. 1).

2 Single field slow-roll inflation

We consider inflationary models with a single scalar field and a standard kinetic term with action [43,44]

$$S = \int d^4x \sqrt{-g} \left[\frac{1}{2} M_{Pl}^2 R - \frac{1}{2} g^{\mu\nu} \partial_\mu \phi \partial_\nu \phi - V(\phi) \right], \quad (1)$$

where $M_{Pl} = (8\pi G)^{-1/2}$ is the reduced Planck mass. The variation of the action with respect to the metric and the scalar field gives the Friedmann equation and the equation of motion of the inflaton,

$$H^2 \equiv \left(\frac{\dot{a}}{a} \right)^2 = \frac{1}{3M_{Pl}^2} \left(\frac{1}{2} \dot{\phi}^2 + V(\phi) \right), \quad (2)$$

$$\ddot{\phi} + 3H\dot{\phi} + \partial_\phi V = 0, \quad (3)$$

where H is the Hubble parameter and we denote with dots and ∂_ϕ the derivatives with respect to time and scalar field,

respectively. The definitions we use for the slow-roll parameters are

$$\epsilon \equiv -\frac{\dot{H}}{H^2}, \quad \eta \equiv \frac{\dot{\epsilon}}{\epsilon H}. \quad (4)$$

3 Local features versus branch features

We consider a single scalar field inflationary model with potential [38]

$$V(\phi) = V_0(\phi) + V_F(\phi), \quad (5)$$

$$V_F(\phi) = \lambda e^{-\left(\frac{\phi-\phi_0}{\sigma}\right)^{2n}}; \quad n > 0, \quad (6)$$

where V_0 is the featureless potential, and we call this type of modification of the slow-roll potential local features (LFs). Many of the features previously studied belong to the category of branch features, which differ from LFs because their definition involves step functions or their smoothed version, which effectively divide the potential in separate branches (Fig. 2).

Some examples of BFs are given by the Starobinsky model [27] or its generalizations [33,35]
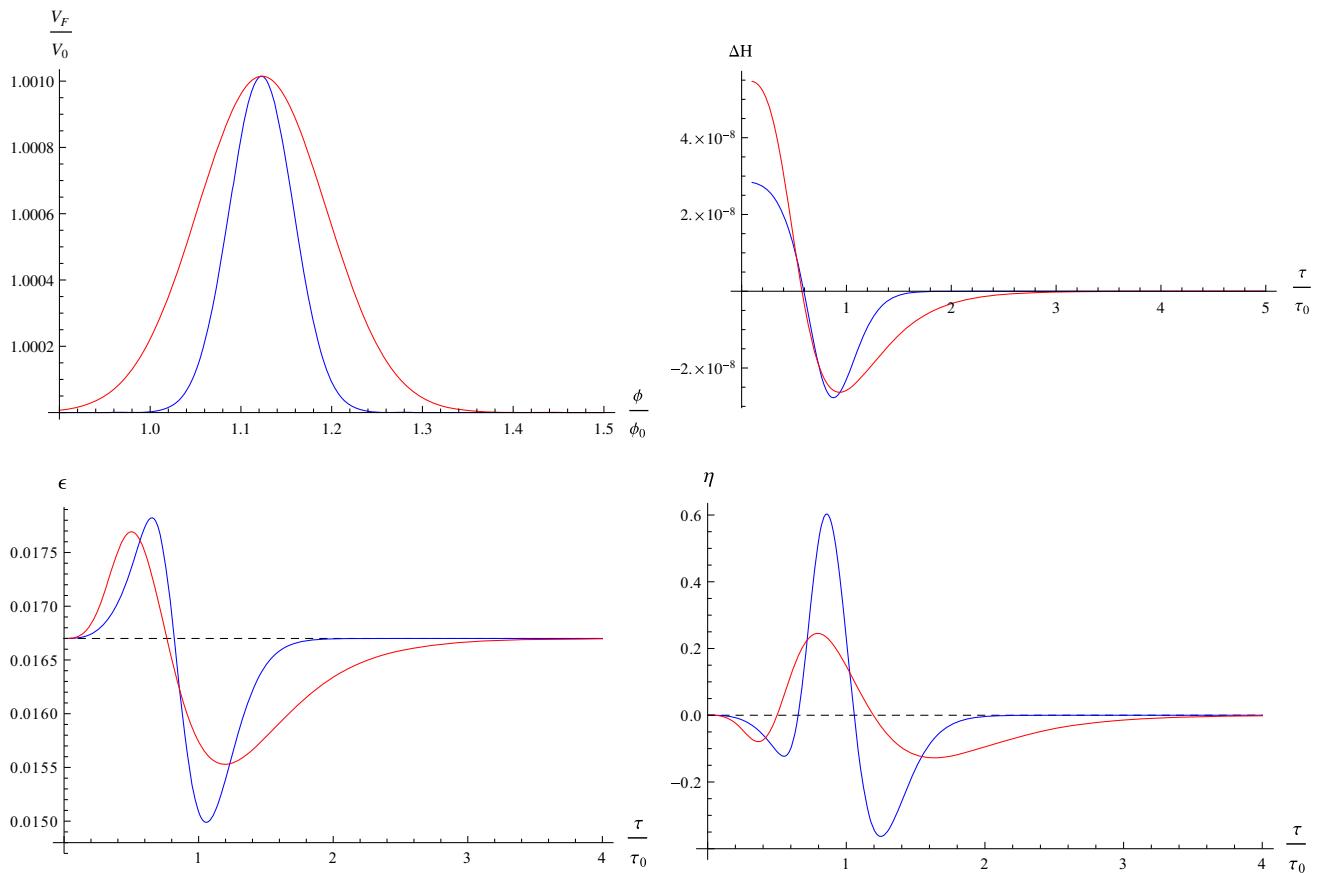
Fig. 2 From *left to right* and *top to bottom* the numerically computed V_F/V_0, ΔH, ϵ, and η are plotted for $\lambda = 10^{-11}$, $\sigma = 0.05$ (*blue*), $\sigma = 0.1$ (*red*), and $n = 1$. The *dashed black lines* correspond to the featureless behavior

$$V_F(\phi) = \lambda(\phi - \phi_0)^n \theta(\phi - \phi_0). \tag{7}$$

The Starobinsky model corresponds to the case $n = 1$, for which an analytical solution was first found in [24,27], and more recently these studies were followed by [32,36]. The type of feature we study in this paper differs from [33] in the fact that here we study only local features, which only affect the potential in a limited range of the field values, while in [33] the features are not local and modify the potential for an entire branch, due to the absence of any dumping factor (Fig. 3).

Some other smoothed versions involving hyperbolic trigonometric function instead of the Heaviside function have also been studied [37]. They can schematically be expressed as

$$V_F(\phi) = \lambda \tanh\left(\frac{\phi - \phi_0}{\Delta}\right). \tag{8}$$

For these models the potential is not only modified around the feature, but for any value in the branch defined by the feature. The direct consequence is that the effects of BFs on perturbation modes are not only visible around the scale k_0 leaving the horizon around the time of the feature, defined

as $\phi(\tau_0) = \phi_0$, but for any scale leaving the horizon when ϕ has a value within the feature branch. This is evident for example from the fact that the spectrum of a BF shows a step around k_0 [45], i.e. the affected scales are all the ones larger (or smaller, depending on the feature) than k_0. On the contrary LFs only affect the perturbation modes which leave the horizon around τ_0, and consequently the spectrum does not show a step, but a local dumped oscillation and it approaches the featureless spectrum for sufficiently smaller and larger scales. This is very important because it could allow one to model local features of the observed spectrum without affecting other scales. The different effects of LFs and BFs on the power spectrum are shown in Fig. 13, where it can be seen that they both produce oscillations qualitatively similar around k_0, but in the case of BFs there is also a step between large and small scales, which is absent for LFs. For BFs if the branches of the feature definition were inverted the role of small and large scales would also be accordingly inverted (Figs. 4 and 5).

In this paper we will consider the case of power-law inflation (PLI) to model the featureless behavior,

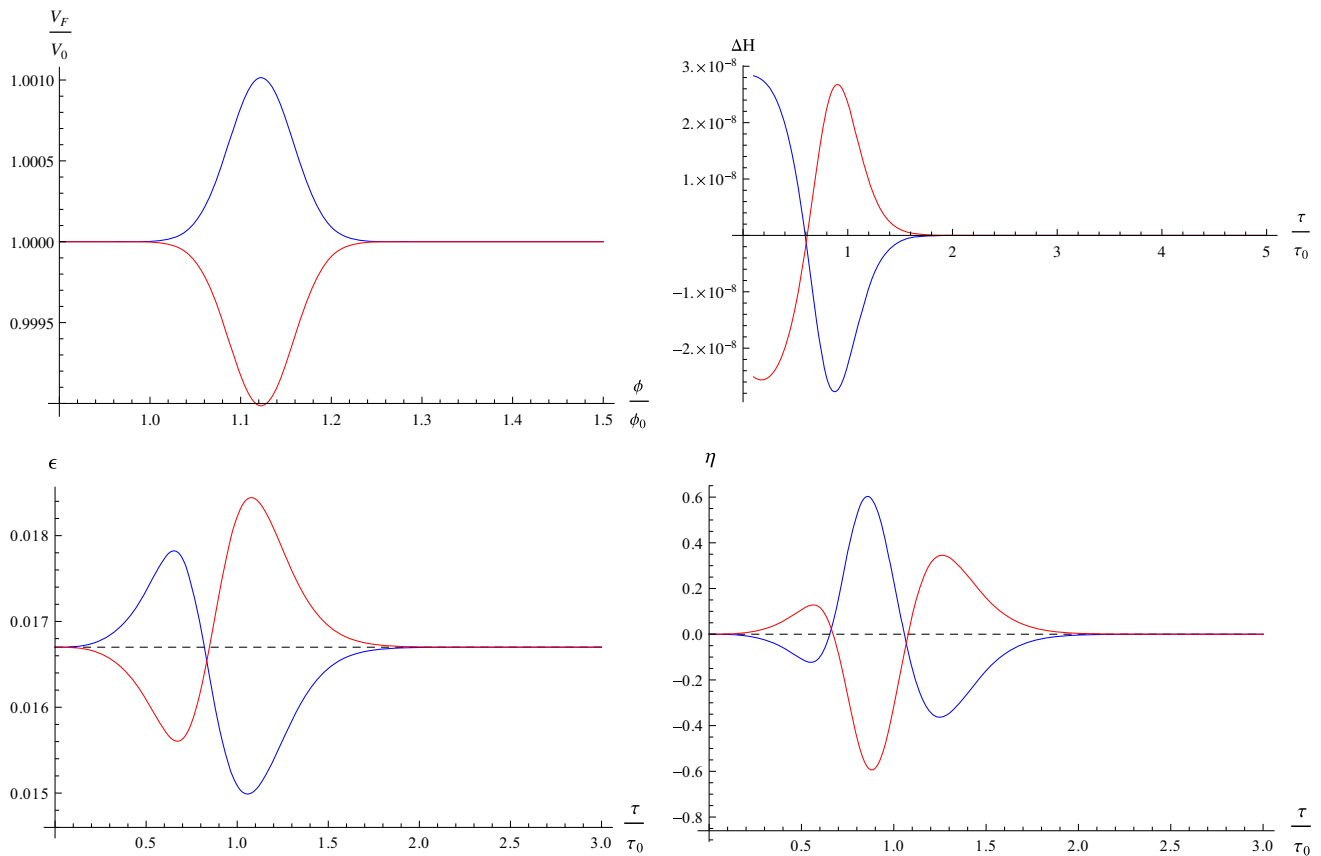$$V_0(\phi) = A e^{-\sqrt{\frac{2}{q}} \frac{\phi}{M_{Pl}}}. \tag{9}$$

Fig. 3 From *left to right* and *top to bottom* the numerically computed V_F/V_0, ΔH, ϵ, and η are plotted for $\lambda = 10^{-11}$ (*blue*) and $-\lambda = 10^{-11}$ (*red*), $\sigma = 0.05$, and $n = 1$. The *dashed black lines* correspond to the featureless behavior

While PLI is not in good agreement with CMB data due to the high value of the predicted tensor-to-scalar ratio r, it can be used as a good toy model to show qualitatively the general type of effect produced by LFs. Future work may be devoted to the test of different potentials $V_0(\phi)$, for direct comparison with the data (Figs. 6, 7, 8, 9, and 10).

4 Local versus branch features effects

One important difference between the effects of BFs and LFs as mentioned earlier is that BFs introduce a step between large and small scales in the spectrum, whose size depends on the featureless model and on the choice of the parameters, in particular λ. The effects of LFs and BFs producing oscillations of comparable size are shown for different potentials in Fig. 13. As it can be seen, depending on the featureless potential $V_0(\phi)$, there can be steps of different size in the spectrum. If λ is very small the effects of BFs and LFs could be phenomenologically indistinguishable, but only a detailed and systematic data analysis can allow one to establish which one of the two categories is observationally preferred, or if they are both compatible with observations (Figs. 11, 12).

Another important difference is that an LF produces *two slow-roll violation phases*, associated to the increasing and decreasing part of the potential feature, while BFs have only one. In this sense a LF can be thought as the superposition of two BFs: for example two smoothed steps with different transition points ϕ_0 and inverted branches are equivalent to one local smoothed step. The distance between the two transition points is related to the LF σ parameter, but each BF has also his own σ parameter controlling the smoothness of each BF transition, so the equivalence is not complete, and there can still be differences between the effects of a LF and appropriate combinations of BFs, as shown in Fig. 14. Schematically, based on general symmetry arguments, we can write

$$V_{\text{LF}}(\phi) \approx V_{\text{BF}}^1(\phi) + V_{\text{BF}}^2(\phi). \tag{10}$$

For example we can approximate a LF as

$$V_{\text{LF}}(\phi) = \lambda e^{-\left(\frac{\phi-\phi_0}{\sigma}\right)^{2n}} \approx V_{\text{BF}}^1(\phi) + V_{\text{BF}}^2(\phi) \tag{11}$$

$$V_{\text{BF}}^1(\phi) = \lambda_1 \tanh\left(\frac{\phi-\phi_1}{\sigma_1}\right),$$

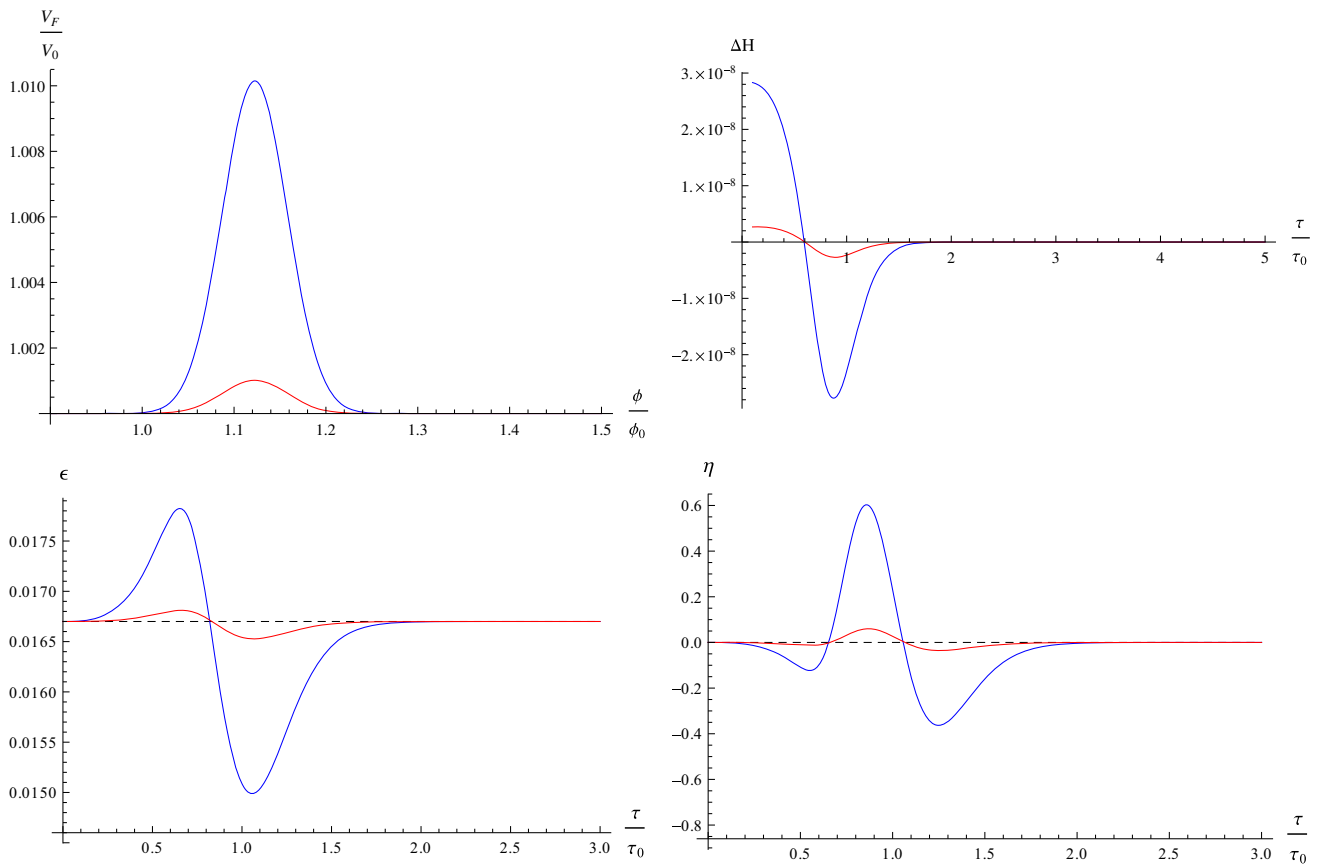$$V_{\text{BF}}^2(\phi) = \lambda_1 \tanh\left(\frac{\phi_2-\phi}{\sigma_1}\right) \tag{12}$$

Fig. 4 From *left to right* and *top to bottom* the numerically computed V_F/V_0, ΔH, ϵ, and η are plotted for $\lambda = 10^{-11}$ (*blue*) and $\lambda = 10^{-12}$ (*red*), $\sigma = 0.05$, and $n = 1$. The *dashed black lines* correspond to the featureless behavior
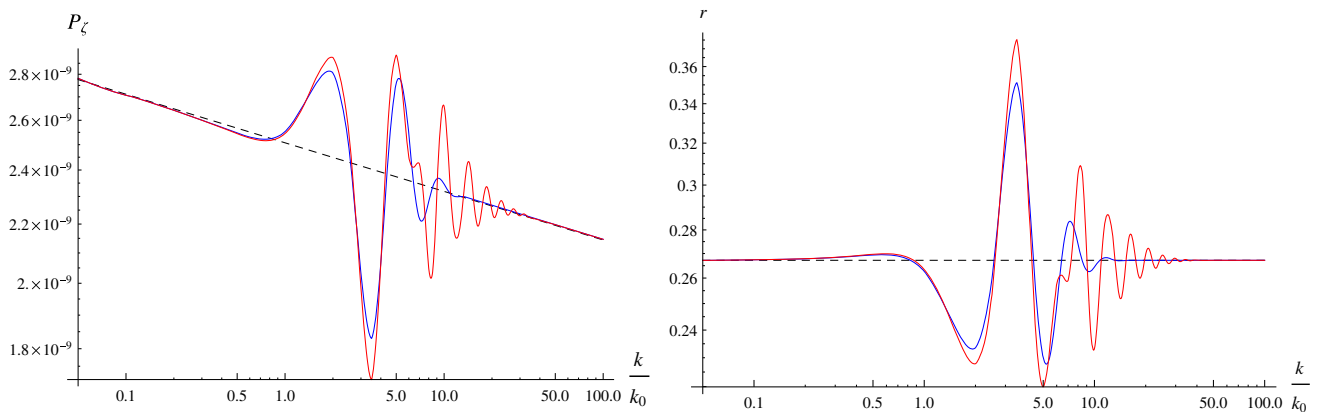

Fig. 5 The numerically computed P_ζ and r are plotted for $\lambda = 10^{-11}$, $\sigma = 0.05$, and $n = 1$ (*blue*) and $n = 2$ (*red*). The *dashed black lines* correspond to the featureless behavior

$$\phi_0 = \frac{\phi_2 + \phi_1}{2}, \quad \lambda = 2\lambda_1, \quad \sigma = \frac{\phi_2 - \phi_1}{2}, \quad \sigma_1 = \frac{\sigma}{2} \qquad (13)$$

Only a systematic analysis of observational data can determine which is the phenomenologically preferred type of feature, but in general a single BF is expected to produce effects different from a single LF, since this is approximately equivalent to the combination of two single BFs (Fig. 13).

5 Curvature perturbations

From now on we adopt a system of units in which $c = \hbar = M_{Pl} = 1$. The study of curvature perturbations is attained by expanding perturbatively the action with respect to the background $FRLW$ solution [46,47]. In the comoving gauge the second and third order actions for scalar perturbations are
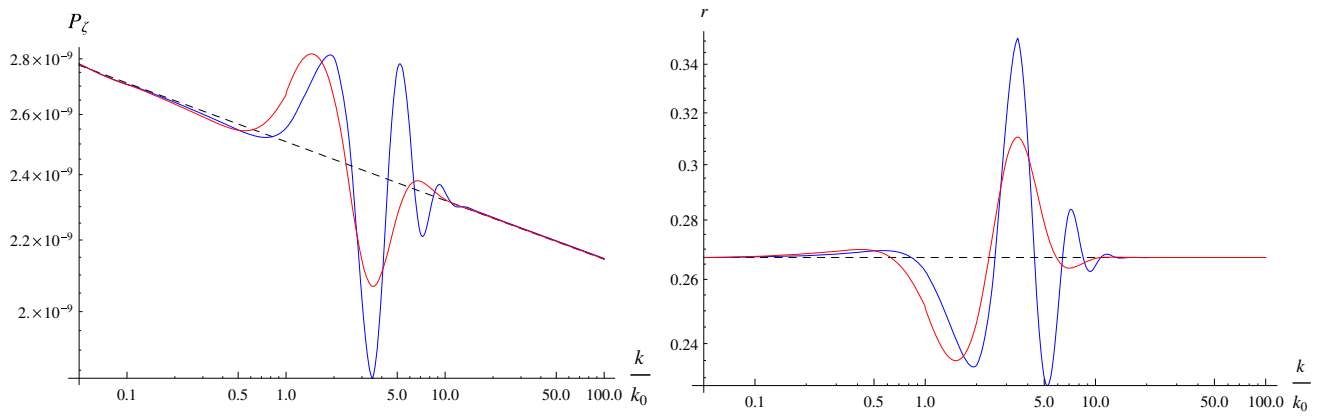
Fig. 6 From *left to right* the numerically computed P_ζ and r are plotted for $\lambda = 10^{-11}$, $\sigma = 0.05$ (*blue*), $\sigma = 0.1$ (*red*), and $n = 1$. The *dashed black lines* correspond to the featureless behavior
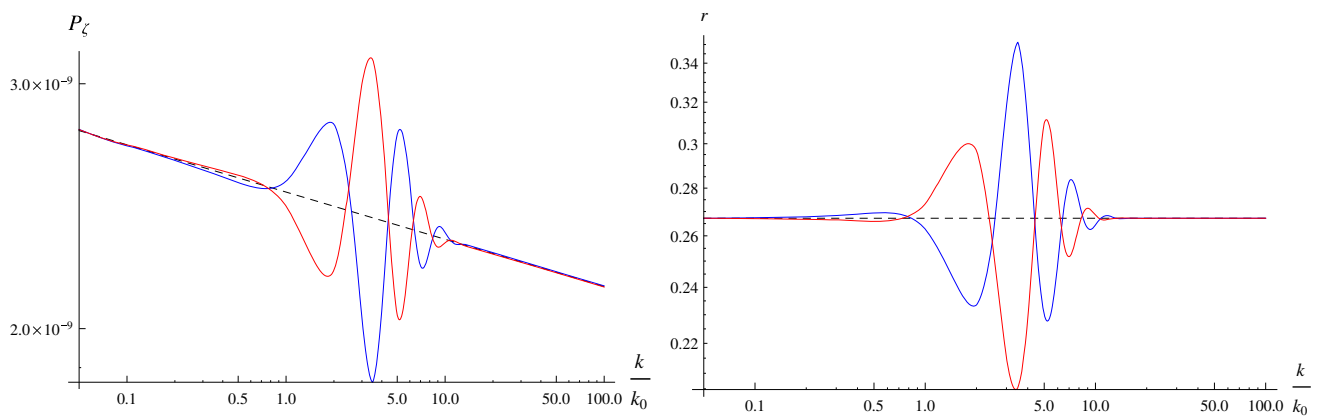

Fig. 7 The numerically computed P_ζ and r are plotted for $\lambda = 10^{-11}$ (*blue*) and $-\lambda = 10^{-11}$ (*red*), $\sigma = 0.05$, and $n = 1$. The *dashed black lines* correspond to the featureless behavior
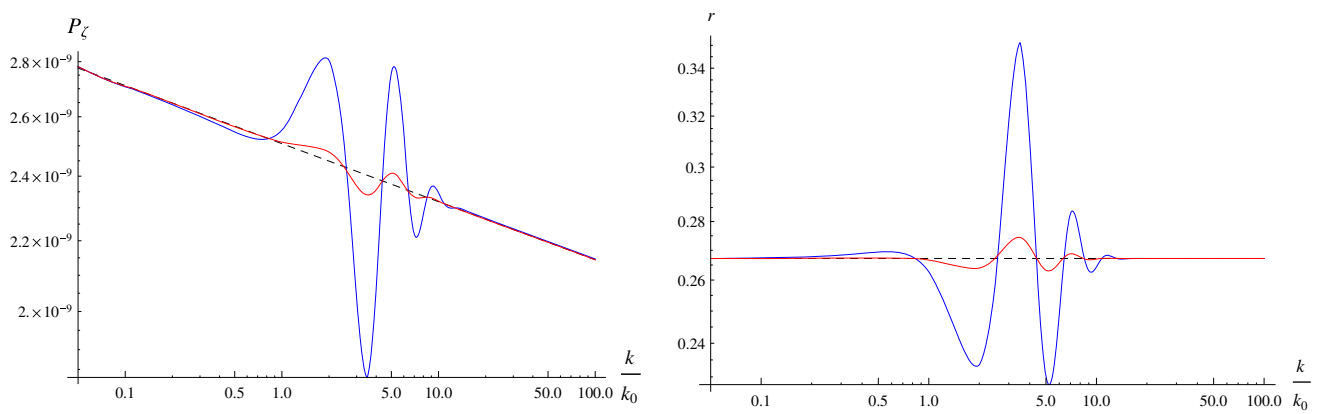

Fig. 8 The numerically computed P_ζ and r are plotted for $\lambda = 10^{-11}$ (*blue*) and $\lambda = 10^{-12}$ (*red*), $\sigma = 0.05$, and $n = 1$. The *dashed black lines* correspond to the featureless behavior
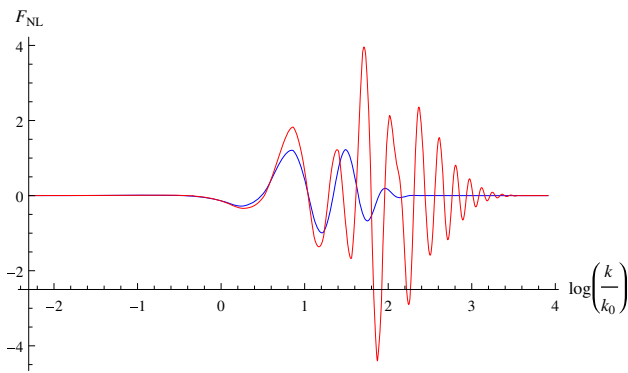
Fig. 9 The numerically computed equilateral shape bispectrum is plotted for $\lambda = 10^{-11}$, $\sigma = 0.05$, and $n = 1$ (*blue*) and $n = 2$ (*red*)
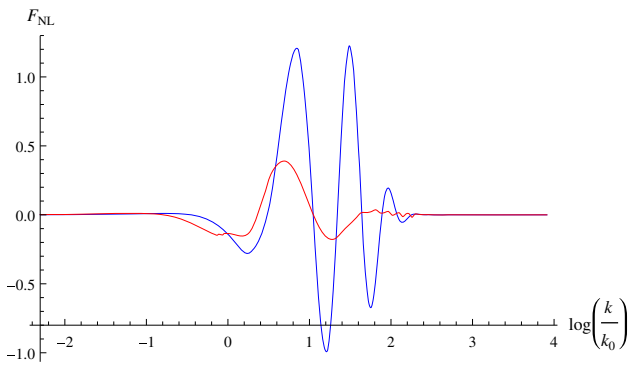

Fig. 10 The numerically computed equilateral shape bispectrum is plotted for $\lambda = 10^{-11}$, $\sigma = 0.05$ (*blue*) $\sigma = 0.1$ (*red*), and $n = 1$
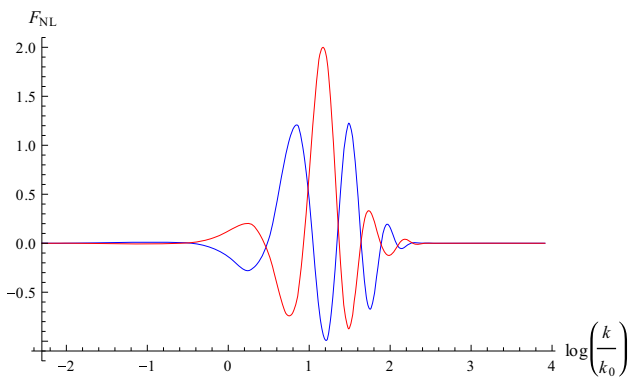

Fig. 11 The numerically computed equilateral shape bispectrum is plotted for $\lambda = 10^{-11}$ (*blue*) and $-\lambda = 10^{-11}$ (*red*), $\sigma = 0.05$, and $n = 1$

$$S_2 = \int \mathrm{d}t \mathrm{d}^3x \left[a^3 \epsilon \dot{\zeta}^2 - a\epsilon(\partial\zeta)^2 \right], \tag{14}$$

$$S_3 = \int \mathrm{d}t \mathrm{d}^3x \left[a^3 \epsilon^2 \zeta \dot{\zeta}^2 + a\epsilon^2 \zeta(\partial\zeta)^2 - 2a\epsilon\dot{\zeta}(\partial\zeta)(\partial\chi) + \frac{a^3\epsilon}{2}\dot{\eta}\zeta^2\dot{\zeta} \right.$$
$$\left. + \frac{\epsilon}{2a}(\partial\zeta)(\partial\chi)\partial^2\chi + \frac{\epsilon}{4a}(\partial^2\zeta)(\partial\chi)^2 + f(\zeta)\frac{\delta L}{\delta\zeta}\Big|_1 \right], \tag{15}$$

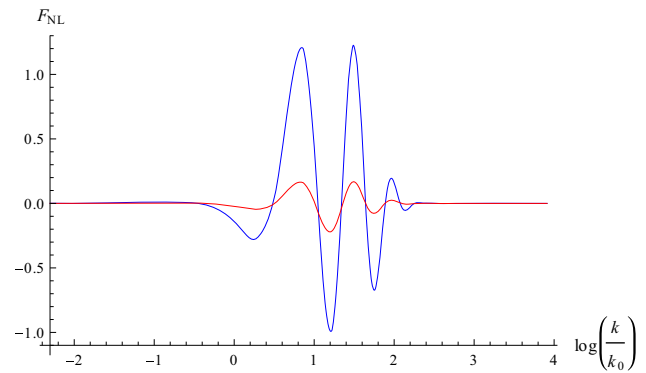**Fig. 12** The numerically computed equilateral shape bispectrum is plotted for $\lambda = 10^{-11}$ (*blue*) and $\lambda = 10^{-12}$ (*red*), $\sigma = 0.05$, and $n = 1$

where

$$\frac{\delta L}{\delta\zeta}\Big|_1 = 2a \left(\frac{\mathrm{d}\partial^2\chi}{\mathrm{d}t} + H\partial^2\chi - \epsilon\partial^2\zeta \right), \tag{16}$$

$$f(\zeta) = \frac{\eta}{4}\zeta + \text{terms with derivatives on } \zeta, \tag{17}$$

and we denote with $\delta L/\delta\zeta|_1$ the variation of the quadratic action with respect to ζ [46]. The Lagrange equations for the second order action give

$$\frac{\partial}{\partial t} \left(a^3 \epsilon \frac{\partial\zeta}{\partial t} \right) - a\epsilon\delta^{ij} \frac{\partial^2\zeta}{\partial x^i \partial x^j} = 0. \tag{18}$$

Taking the Fourier transform and using the conformal time $\mathrm{d}\tau \equiv \mathrm{d}t/a$ we obtain

$$\zeta_k'' + 2\frac{z'}{z}\zeta_k' + k^2\zeta_k = 0, \tag{19}$$

where $z \equiv a\sqrt{2\epsilon}$, k is the comoving wave number, and primes denote derivatives with respect to the conformal time.

A similar approach can be adopted for the perturbations of the tensor modes h_k, which satisfy the equation

$$h_k'' + 2\frac{a'}{a}h_k' + k^2 h_k = 0. \tag{20}$$

The power spectrum of scalar perturbations is the Fourier transform of the two-point correlation function of ζ. For the power spectrum of scalar perturbations we adopt the definition

$$P_\zeta(k) \equiv \frac{2k^3}{(2\pi)^2}|\zeta_k|^2, \tag{21}$$
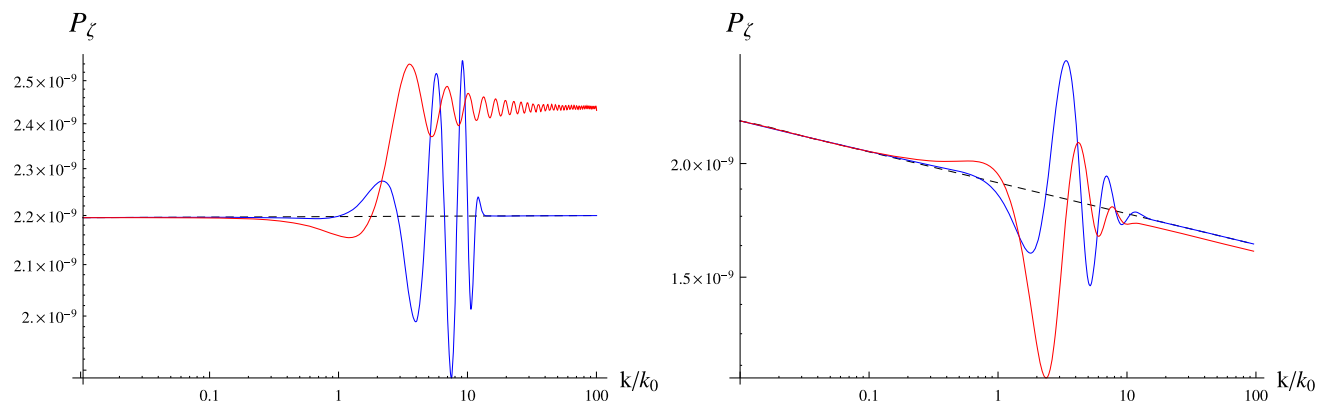
and for the power spectrum of tensor perturbations

Fig. 13 The numerically computed power spectra are plotted as a function of k/k_0 for different potentials. The *dashed lines* are the spectra for the featureless potential $V_0(\phi)$, the *blue lines* are for the spectrum corresponding to a LF, and the *red lines* to a BF. On the *left* we have $V_0(\phi) = V_{vac} + \frac{1}{2}m^2\phi^2$, where $V_{vac} = 3.3 \times 10^{-13} M_{pl}^3$ and $m = 6 \times 10^{-9} M_{pl}$. For a LF the potential is $V(\phi) = V_0(\phi) + \lambda e^{-(\frac{\phi-\phi_0}{\sigma})^2}$, with $\lambda = 6.5 \times 10^{-21}$, $\sigma = 10^{-4}$, while the BF is of the type studied before in [33] corresponding to $V(\phi) = V_0(\phi) + \lambda\theta(\phi_0 - \phi)$, with $\lambda = -10^{-16}$. On the *right* we have $V_0(\phi) = Ae^{-\sqrt{\frac{2}{q}}\frac{\phi}{M_{Pl}}}$, the power-law potential. For a LF the potential is $V(\phi) = V_0(\phi) + \lambda e^{-(\frac{\phi-\phi_0}{\sigma})^2}$,

with $\lambda = -10^{-11}$ and $\sigma = 0.05$, while the BF corresponds to $V(\phi) = V_0(\phi) + \frac{\lambda}{2}[1 + \tanh(\frac{\phi_0 - \phi}{\sigma})]$, with $\lambda = -3 \times 10^{-11}$ and $\sigma = 0.05$. The parameters have been chosen so that the different types of features produce oscillations of similar size, so that the effects can be compared consistently. As it can be seen, depending on the featureless potential V_0, there are cases in which the step between the large and small scale spectrum produced by BFs can be important. The oscillation patterns can also be different, since a single BF has only one phase of slow-roll violation, while in a single LF there are two slow-roll violation phases, corresponding to the increasing and decreasing part of the feature
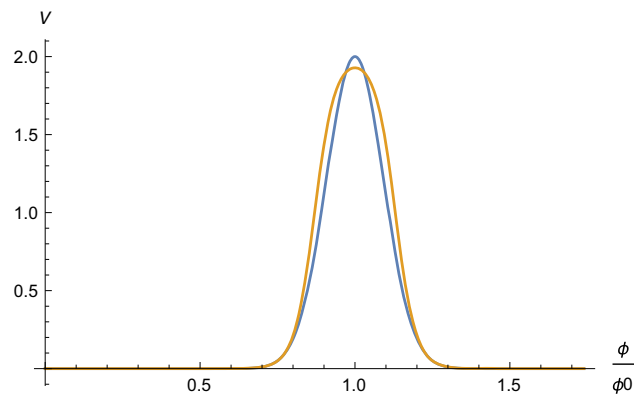
6 Calculation of the bispectrum of curvature perturbation

The bispectrum B_ζ is defined as the Fourier transform of the three-point correlation function as

$$\langle \zeta(\vec{k}_1, t)\zeta(\vec{k}_2, t)\zeta(\vec{k}_3, t)\rangle = (2\pi)^3 B_\zeta(k_1, k_2, k_3)\delta^{(3)}(\vec{k}_1 + \vec{k}_2, \vec{k}_3). \tag{24}$$

After a field redefinition, we can re-write the third order action as

$$S_3 = \int dt d^3x \left[-a^3\epsilon\eta\zeta\dot{\zeta}^2 - \frac{1}{2}a\epsilon\eta\zeta\partial^2\zeta \right], \tag{25}$$

from which the interaction Hamiltonian can be written in terms of the conformal time as

$$H_{int}(\tau) = \int d^3x\,\epsilon\eta a \left[\zeta\zeta'^2 + \frac{1}{2}\zeta^2\partial^2\zeta \right]. \tag{26}$$

Finally, the three-point correlation function is given by [46, 48]

$$\langle\Omega|\zeta(\tau_e, \vec{k}_1)\zeta(\tau_e, \vec{k}_2)\zeta(\tau_e, \vec{k}_3)|\Omega\rangle$$
$$= -i \int_{-\infty}^{\tau_e} \left\langle 0 \left| \left[\zeta(\tau_e, \vec{k}_1)\zeta(\tau_e, \vec{k}_2)\zeta(\tau_e, \vec{k}_3), H_{int} \right] \right| 0 \right\rangle. \tag{27}$$

After substitution we get

Fig. 14 The local feature potential V_{LF} in Eq. (11) and its approximation as the sum of two BF potentials $V_{BF}^1(\phi) + V_{BF}^2(\phi)$ defined in Eq. (12) are plotted, respectively, in *blue* and in *light brown* around ϕ_0 for $\phi_1 = 1$, $\phi_2 = 1.2$, $\lambda_1 = 1$, and $n = 1$. This is an example of the fact that appropriate combinations of two BFs can produce modifications of the potential similar to a local feature

$$P_h(k) \equiv \frac{2k^3}{\pi^2}|h_k|^2. \tag{22}$$

The tensor-to-scalar ratio is defined as the ratio between the spectrum of tensor and scalar perturbations

$$r \equiv \frac{P_h}{P_\zeta}. \tag{23}$$

$$B_\zeta(k_1, k_2, k_3) = 2\Im\Bigg[\zeta(\tau_e, k_1)\zeta(\tau_e, k_2)\zeta(\tau_e, k_3)$$

$$\times \int_{\tau_i}^{\tau_e} d\tau\, \eta\epsilon a^2 \Big(2\zeta^*(\tau, k_1)\zeta'^*(\tau, k_2)\zeta'^*(\tau, k_3)$$

$$-k_1^2\zeta^*(\tau, k_1)\zeta^*(\tau, k_2)\zeta^*(\tau, k_3)\Big)$$

$$+ \text{two permutations of } k_1, k_2, \text{ and } k_3 \Bigg], \qquad (28)$$

where $\Im$ is the imaginary part. The integral is computed from τ_i to τ_e, where τ_i is some time before τ_0 when the feature effects on the background and perturbations evolution start to be important, and τ_e is some time after the horizon crossing, when the modes have frozen [49–53] (Fig. 14).

A commonly used quantity introduced to study non-Gaussianity is the parameter $f_{\rm NL}$

$$\frac{6}{5}f_{\rm NL}(k_1, k_2, k_3) \equiv \frac{B_\zeta}{\mathbf{P}_\zeta(k_1)\mathbf{P}_\zeta(k_2) + \mathbf{P}_\zeta(k_1)\mathbf{P}_\zeta(k_3) + \mathbf{P}_\zeta(k_2)\mathbf{P}_\zeta(k_3)}, \qquad (29)$$

where

$$\mathbf{P}_\zeta \equiv \frac{2\pi^2}{k^3}P_\zeta. \qquad (30)$$

After replacing $\mathbf{P}_\zeta$ in Eq. (29) we can obtain $f_{\rm NL}$ in terms of our definition of the spectrum $P_\zeta(k)$

$$f_{\rm NL}(k_1, k_2, k_3)$$
$$= \frac{10}{3}\frac{(k_1 k_2 k_3)^3}{(2\pi)^4}\frac{B_\zeta}{P_\zeta(k_1)P_\zeta(k_2)k_3^3 + P_\zeta(k_1)P_\zeta(k_3)k_2^3 + P_\zeta(k_2)P_\zeta(k_3)k_1^3}. \qquad (31)$$

In this paper we will use a different quantity to study non-Gaussianity

$$F_{\rm NL}(k_1, k_2, k_3; k_*) \equiv \frac{10}{3(2\pi)^4}\frac{(k_1 k_2 k_3)^3}{k_1^3 + k_2^3 + k_3^3}\frac{B_\zeta(k_1, k_2, k_3)}{P_\zeta^2(k_*)}, \qquad (32)$$

where k_* is the pivot scale at which the power spectrum is normalized, i.e. $P_\zeta(k_*) \approx 2.2 \times 10^{-9}$. When the spectrum is approximately scale invariant our definition of $F_{\rm NL}$ reduces to $f_{\rm NL}$ in the equilateral limit, but in general $f_{\rm NL}$ and $F_{\rm NL}$ are not the same. For example in the squeezed limit they are different, but $F_{\rm NL}$ still provides useful information as regards the non-Gaussian behavior of B_ζ.

7 Effects of the parameter n

7.1 Background

The parameter n is related to the dumping of the feature, and larger values are associated to a steeper change of the potential, as shown in Fig. 1. The slow-roll parameters show an oscillation around the feature time τ_0 with a larger amplitude for larger n, since a steeper potential change is also associated to larger derivatives of the Hubble parameter as shown in Fig. 1. To better understand the effects on the slow-roll parameter we define the quantity

$$\Delta H = H_F - H_0, \qquad (33)$$

where H_F is the Hubble parameter for the model with a feature, and H_0 is for the featureless model. From the definition in Eq. (4) we can easily see that at leading order in ΔH we have

$$\epsilon_F = \epsilon_0 + \Delta\epsilon, \qquad (34)$$

$$\Delta\epsilon \approx -\frac{\partial_t \Delta H}{H_0^2}, \qquad (35)$$

where we have defined

$$\epsilon_F = -\frac{\dot{H}_F}{H_F^2}, \qquad (36)$$

$$\epsilon_0 = -\frac{\dot{H}_0}{H_0^2}. \qquad (37)$$

The temporary violation of slow-roll conditions comes from the time derivative of ΔH, so even small changes in the expansion history of the Universe can produce important non-Gaussianities if they happen sufficiently fast. In the limit of very large n the feature of the potential tends to a local bump characterized by a very steep transition.

7.2 Perturbations

As shown in Fig. 5 the tensor-to-scalar ratio r and the spectrum of primordial curvature perturbations show oscillations around the scale $k_0 = -1/\tau_0$ with an amplitude which increases for larger n. We can understand this from the behavior of ΔH, which has a larger time derivative for larger n, because the transition for the potential is also steeper. As seen in Fig. 9 the equilateral limit of the bispectrum also shows oscillations around k_0, which are larger for larger n, for the same reason given above. It is important to observe that both the spectrum and the bispectrum are only affected in a limited range of scales, since this is a LF. For a BF, instead, the change affects all the scales before of after the feature [33,45], because the potential is modified in the entire branch.

8 Effects of the parameter σ

8.1 Background

The parameter σ determines the size of the range of field values where the potential is affected by the feature, as shown

in Fig. 2. The slow-roll parameters are smaller for larger σ since a larger width of the feature tend to reduce the time derivative of the Hubble parameter. In this case, in fact, the modification of the potential is also associated to smaller derivatives with respect to the field, since the shape of the potential is less steep.

8.2 Perturbations

As shown in Fig. 6 the spectrum of primordial curvature perturbations and the tensor-to-scalar ratio r have oscillations around k_0, whose amplitude is larger for smaller σ, because in this case the potential changes faster and consequently the slow-roll parameters are larger. In Fig. 10 we can see that the equilateral limit of the bispectrum also presents oscillations around k_0 with larger amplitude for smaller σ. Both for the spectrum and bispectrum the effects are confined in a limited range of the scales, differently from what we would have with BFs.

9 Effects of the parameter λ

9.1 Background

The parameter λ controls the magnitude of the potential modification, as shown in Figs. 3 and 4. For larger absolute values of λ, the slow-roll parameters are larger in absolute value, since a larger feature of the potential induces a larger time derivative of the Hubble parameter. The sign of λ produce opposite and symmetric effects, since it implies an opposite sign for the derivative of the potential with respect to the field, and consequently of the Hubble parameter with respect to time.

9.2 Perturbations

As shown in Figs. 7, 8, 11, 12, larger absolute values of λ produce oscillations with a larger amplitude for the tensor-to-scalar ratio r, the spectrum and bispectrum around k_0. Features with the same absolute value and opposite sign of λ correspond to oscillations that are symmetric with respect to the featureless spectrum and bispectrum.

10 Effects on the CMB temperature and polarization spectrum

In this section we present the effects of the feature on the CMB temperature and polarization spectrum. To study how the feature impacts on the CMB spectra we modified the Boltzmann equations solver Code for Anisotropies in the Microwave Background (CAMB) [54] to use the modified

primordial power spectrum instead of the usual power-law expression $P_s(k) = A_s (k/0.05 \, \mathrm{Mpc}^{-1})^{n_s - 1}$, where A_s is the normalization and n_s is the tilt of the power-law spectrum.

The CMB spectrum is the convolution of the power spectrum of initial perturbations with the transfer function, which is calculated by CAMB assuming the standard cosmological model. We fix all the cosmological parameters to the Planck 2015 best-fit values [4].

In Figs. 15, 16, 17, and 18 we show the CMB spectra obtained with different combinations of the parameters λ, σ, and n: in Table 1 we list the values of the feature parameters for each combination. We show the spectra in terms of the quantity $D_\ell = \ell(\ell + 1)C_\ell/(2\pi)$. For each of the temperature (TT, Fig. 15), E-mode polarization (EE, Fig. 17), and B-mode polarization (BB, Fig. 18) auto-correlation power spectra we plot the D_ℓ spectra (top) and the relative difference with respect to the featureless spectrum (bottom) for a large range of multipoles. In Fig. 16 we show also the TE cross-correlation power spectra. The spectra are compared with the most recent experimental data: we plot the Planck data [55] for the TT, TE, and EE spectra and the points obtained by the SPTPol experiment [56] and the Bicep–Keck (BK) collaboration [57] data for the BB spectrum. The SPTPol data provide the first detection of the B modes generated by the lensing of E-mode perturbations. We recall that the BK data plotted here contain a significant contamination from B modes emitted by dust [58].

From the various plots it is possible to see how the feature can change the predicted CMB spectra. In particular, the most significant variations are in the TT and in the EE spectra, where relative differences of the order of 10–15 % are visible, while the presence of the feature has a very small impact on the B-mode spectrum. Choosing the values listed in Table 1 for the parameters describing the feature, and $k_0 = 5 \times 10^{-4} \, \mathrm{Mpc}^{-1}$, $A_s = 2.2 \times 10^{-9}$, and $n_s = 0.967$ we can see from Fig. 15 that the effects of some feature can partially reproduce the dip at $\ell \simeq 20$ in the TT spectrum. Further studies involving data fitting can determine more accurately the values of the parameters which provide the best explanation of the observed deviation of the power spectrum from the power-law form, but they go beyond the scope of this paper, and they will be reported separately. From Figs. 15, 16, 17, and 18 it is also clear that the presence of the LF affects only a part of the CMB spectra, while far from the multipoles corresponding to the feature scale the spectra are equal to those obtained in the featureless case.

11 Conclusions

We have studied the effects of local features of the inflaton potential on the spectrum and bispectrum of single field inflationary models with a canonical kinetic term. These features
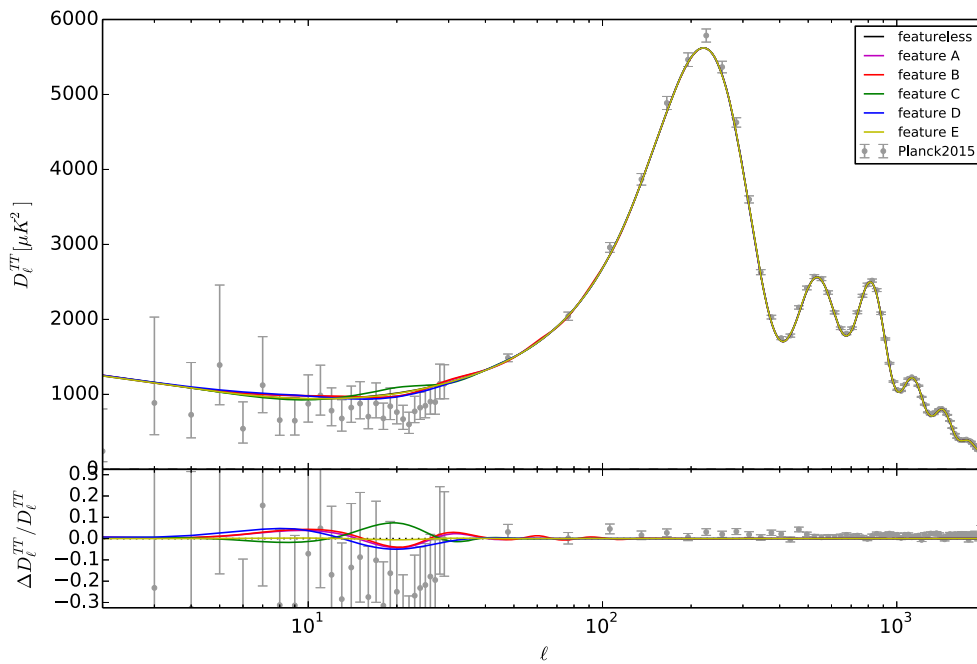
Fig. 15 We plot the $D_l^{TT} = \ell(\ell+1)C_\ell^{TT}/(2\pi)$ spectrum in units of μK^2 with respect to the multipole l, and the relative difference with respect to the featureless behavior. The *solid black lines* correspond to the featureless behavior. The values of λ, σ, and n we used for the different curves are listed in Table 1
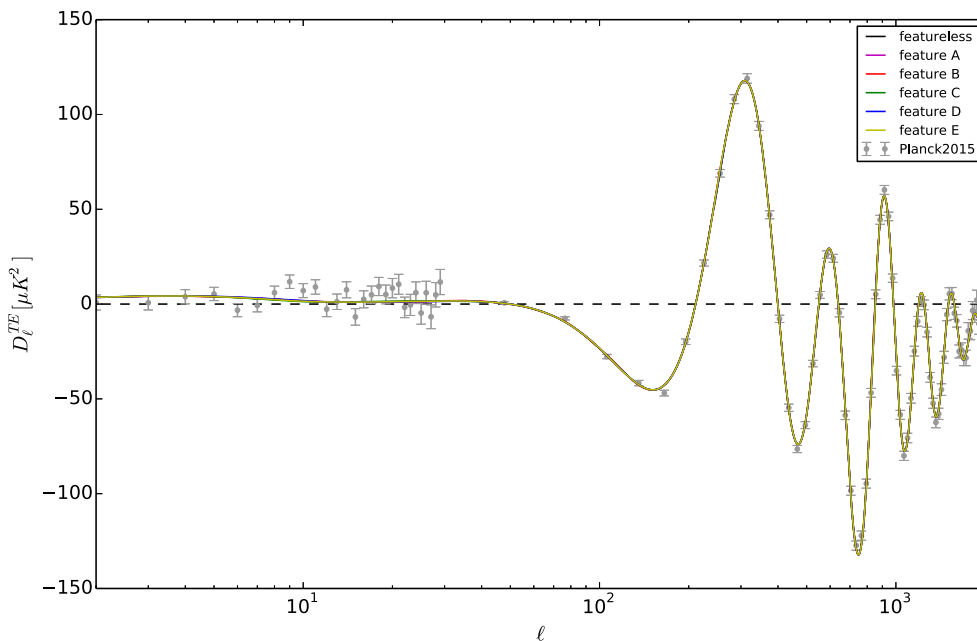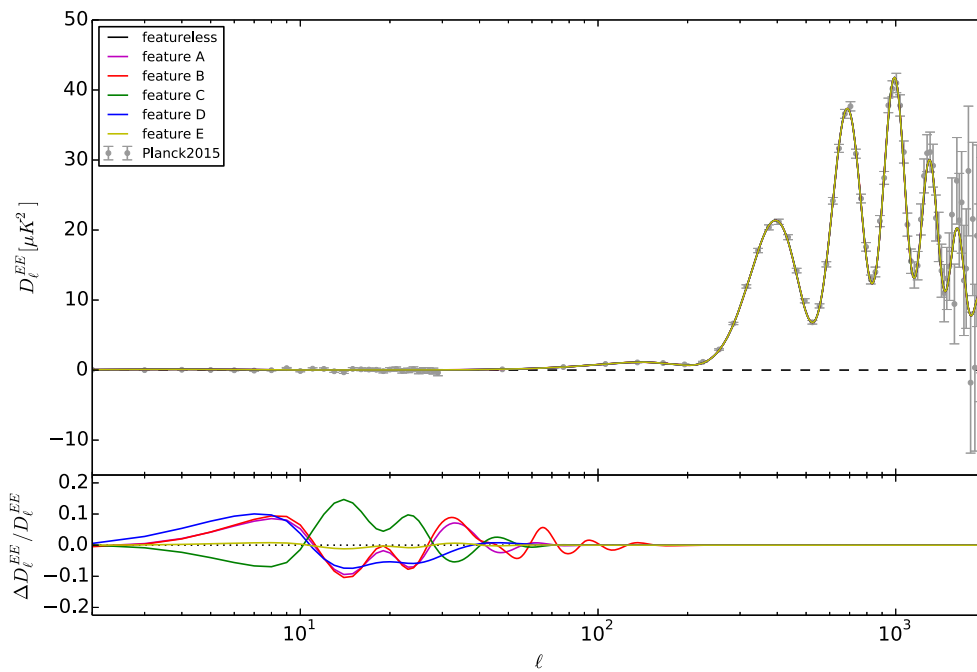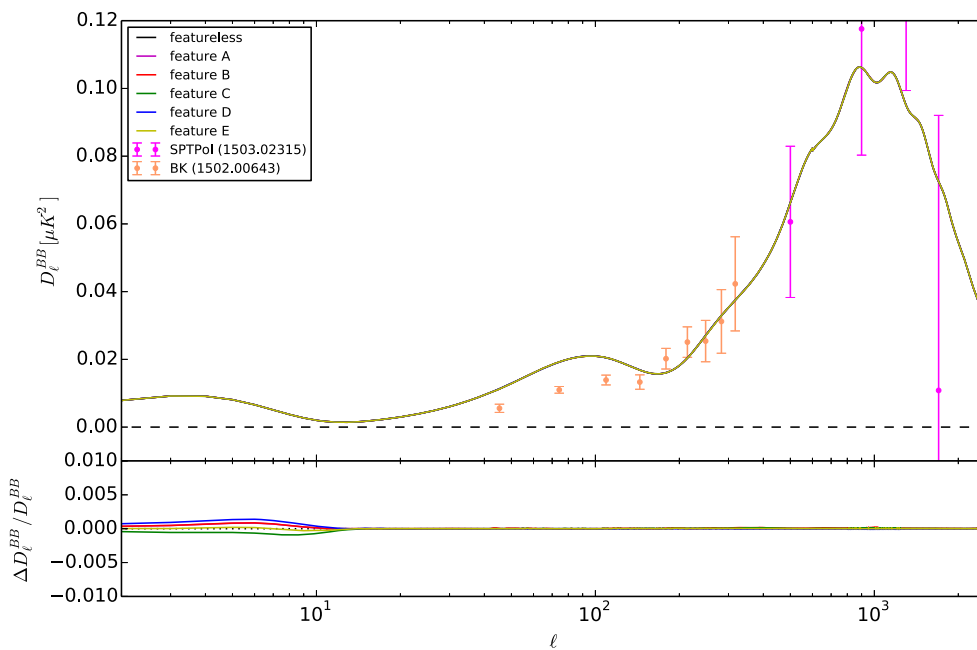

Fig. 16 We plot the $D_l^{TE} = \ell(\ell+1)C_\ell^{TE}/(2\pi)$ spectrum in units of μK^2 with respect to the multipole l. The *solid black lines* correspond to the featureless behavior. The values of λ, σ, and n we used for the different curves are listed in Table 1

only modify the potential in a limited range of the scalar field values, and consequently only affect the spectrum and bispectrum in a narrow range of scales, which leave the horizon during the time interval corresponding to the modification of the potential. This is different from branch-type features which effectively divide the potential into separate branches, because they involve a step-like function in their definition. Some examples of branch-type features are the Starobinsky model [27] and its generalizations [33,35]. In BF models the spectrum can, for example, exhibit a step,

Fig. 17 We plot the $D_l^{EE} = \ell(\ell + 1)C_\ell^{EE}/(2\pi)$ spectrum in units of μK^2 with respect to the multipole l, and the relative difference with respect to the featureless behavior. The *solid black lines* correspond to the featureless behavior. The values of λ, σ, and n we used for the different curves are listed in Table 1

Fig. 18 We plot the $D_l^{BB} = \ell(\ell + 1)C_\ell^{BB}/(2\pi)$ spectrum in units of μK^2 with respect to the multipole l, and the relative difference with respect to the featureless behavior. The *solid black lines* correspond to the featureless behavior. The values of λ, σ, and n we used for the different curves are listed in Table 1

reminiscent of the branch-type potential modifications. For local features there is no step, and the spectrum returns to the featureless form for scales sufficiently larger or smaller than k_0.

The tensor-to-scalar ratio r, the spectrum, and the bispectrum of primordial curvature perturbations are affected by the feature, showing modulated oscillations which are dumped for scales larger or smaller than k_0. The amplitude of the oscil-

Table 1 The values of λ, σ, and n we used for the different spectra in Figs. 15, 16, 17, 18

Label	λ	σ	n
Feature A	10^{-11}	0.05	1
Feature B	10^{-11}	0.05	2
Feature C	-10^{-11}	0.05	1
Feature D	10^{-11}	0.1	1
Feature E	10^{-12}	0.05	1

lations depends on the parameters defining the local feature, and the effects are larger when the potential modification is steeper, since in this case there is a stronger violation of the slow-roll conditions.

We have also computed the effects of the features on the CMB temperature and polarization spectra, showing how an appropriate choice of parameters can produce effects in qualitative agreement with the observational CMB data. Due to this local-type effect these features could be used to model phenomenologically local glitches of the spectrum, without affecting other scales, and it will be interesting in the future to perform a detailed observational data fitting analysis using the new CMB data of the Planck mission.

References

1. E. Komatsu et al., (2009). arXiv:0902.4759
2. WMAP, G. Hinshaw et al., Astrophys. J. Suppl. **208**, 19 (2013). arXiv:1212.5226
3. Planck Collaboration, P. Ade et al., (2013). arXiv:1303.5076
4. Planck, P.A.R. Ade et al., (2015). arXiv:1502.01589
5. A.A. Starobinsky, Phys. Lett. B **91**, 99 (1980)
6. J. Martin, C. Ringeval, V. Vennin, (2013). arXiv:1303.3787
7. A. Shafieloo, T. Souradeep, Phys. Rev. D **70**, 043523 (2004). arXiv:astro-ph/0312174
8. G. Nicholson, C.R. Contaldi, JCAP **0907**, 011 (2009). arXiv:0903.1106
9. D.K. Hazra, A. Shafieloo, T. Souradeep, Phys. Rev. D **87**, 123528 (2013). arXiv:1303.5336
10. D.K. Hazra, A. Shafieloo, T. Souradeep, JCAP **1411**, 011 (2014). arXiv:1406.4827
11. G. Nicholson, C.R. Contaldi, P. Paykari, JCAP **1001**, 016 (2010). arXiv:0909.5092
12. P. Hunt, S. Sarkar, JCAP **1401**, 025 (2014). arXiv:1308.2317
13. P. Hunt, S. Sarkar, (2015). arXiv:1510.03338
14. G. Goswami, J. Prasad, Phys. Rev. D **88**, 023522 (2013). arXiv:1303.4747
15. M. Matsumiya, M. Sasaki, J. Yokoyama, Phys. Rev. D **65**, 083007 (2002). arXiv:astro-ph/0111549
16. M. Matsumiya, M. Sasaki, J. Yokoyama, JCAP **0302**, 003 (2003). arXiv:astro-ph/0210365
17. N. Kogo, M. Matsumiya, M. Sasaki, J. Yokoyama, Astrophys. J. **607**, 32 (2004). arXiv:astro-ph/0309662
18. N. Kogo, M. Sasaki, J. Yokoyama, Prog. Theor. Phys. **114**, 555 (2005). arXiv:astro-ph/0504471
19. R. Nagata, J. Yokoyama, Phys. Rev. D **78**, 123002 (2008). arXiv:0809.4537
20. Planck Collaboration, P. Ade et al., (2015). arXiv:1502.02114
21. S. Gariazzo, C. Giunti, M. Laveder, JCAP **1504**, 023 (2015). arXiv:1412.7405
22. E. Di Valentino, S. Gariazzo, E. Giusarma, O. Mena, Phys. Rev. D **91**, 123505 (2015). arXiv:1503.00911
23. D.K. Hazra, A. Shafieloo, G.F. Smoot, A.A. Starobinsky, JCAP **1406**, 061 (2014). arXiv:1403.7786
24. A.A. Starobinsky, JETP Lett. **55**, 489 (1992)
25. J. Hamann, L. Covi, A. Melchiorri, A. Slosar, Phys. Rev. D **76**, 023503 (2007). arXiv:astro-ph/0701380
26. D.K. Hazra, M. Aich, R.K. Jain, L. Sriramkumar, T. Souradeep, JCAP **1010**, 008 (2010). arXiv:1005.2175
27. A.A. Starobinsky, Grav. Cosmol. **4**, 88 (1998). arXiv:astro-ph/9811360
28. M. Joy, V. Sahni, A.A. Starobinsky, Phys. Rev. D **77**, 023514 (2008). arXiv:0711.1585
29. M. Joy, A. Shafieloo, V. Sahni, A.A. Starobinsky, JCAP **0906**, 028 (2009). arXiv:0807.3334
30. M.J. Mortonson, C. Dvorkin, H.V. Peiris, W. Hu, Phys. Rev. D **79**, 103519 (2009). arXiv:0903.4920
31. C.P. Novaes, M. Benetti, A. Bernui, (2015). arXiv:1507.01657
32. R. Bousso, D. Harlow, L. Senatore, Phys. Rev. D **91**, 083527 (2015). arXiv:1309.4060
33. A.G. Cadavid, A.E. Romano, Eur. Phys. J. C **75**, 589 (2015). arXiv:1404.2985
34. A. Gallego Cadavid, A.E. Romano, Nucl. Part. Phys. Proc. **267–269**, 254 (2015)
35. D.K. Hazra, A. Shafieloo, G.F. Smoot, A.A. Starobinsky, Phys. Rev. Lett. **113**, 071301 (2014). arXiv:1404.0360
36. D.K. Hazra, A. Shafieloo, G.F. Smoot, A.A. Starobinsky, JCAP **1408**, 048 (2014). arXiv:1405.2012
37. J.A. Adams, B. Cresswell, R. Easther, Phys. Rev. D **64**, 123514 (2001). arXiv:astro-ph/0102236
38. A. Gallego Cadavid, Primordial non-Gaussianities produced by features in the potential of single slow-roll inflationary models. Master's thesis, University of Antioquia, 2013. arXiv:1508.05684
39. G.A. Palma, JCAP **1504**, 035 (2015). arXiv:1412.5615
40. S. Mooij, G.A. Palma, G. Panotopoulos, A. Soto, JCAP **1510**, 062 (2015). arXiv:1507.08481 [Erratum: JCAP1602, no.02, E01(2016)]
41. A.E. Romano, M. Sasaki, Phys. Rev. D **78**, 103522 (2008). arXiv:0809.5142
42. J.A. Adams, G.G. Ross, S. Sarkar, Nucl. Phys. B **503**, 405 (1997). arXiv:hep-ph/9704286
43. D. Langlois, Lect. Notes Phys. **800**, 1 (2010). arXiv:1001.5259
44. A.R. Liddle, D.H. Lyth, *Cosmological Inflation and Large Scale Structure* (Cambridge University Press, Cambridge, 2000)

45. F. Arroja, A.E. Romano, M. Sasaki, Phys. Rev. D **84**, 123503 (2011). arXiv:1106.5384
46. J.M. Maldacena, JHEP **0305**, 013 (2003). arXiv:astro-ph/0210603
47. H. Collins, (2011). arXiv:1101.1308
48. X. Chen, Adv. Astron. **2010**, 638979 (2010). arXiv:1002.1416
49. P. Adshead, C. Dvorkin, W. Hu, E.A. Lim, Phys. Rev. D **85**, 023531 (2012). arXiv:1110.3050
50. X. Chen, R. Easther, E.A. Lim, JCAP **0706**, 023 (2007). arXiv:astro-ph/0611645
51. X. Chen, R. Easther, E.A. Lim, JCAP **0804**, 010 (2008). arXiv:0801.3295
52. D.K. Hazra, L. Sriramkumar, J. Martin, JCAP **5**, 26 (2013). arXiv:1201.0926
53. V. Sreenath, R. Tibrewala, L. Sriramkumar, JCAP **12**, 37 (2013). arXiv:1309.7169
54. A. Lewis, A. Challinor, A. Lasenby, Astrophys. J. **538**, 473 (2000). arXiv:astro-ph/9911177
55. Planck, R. Adam et al., (2015). arXiv:1502.01582
56. R. Keisler et al., Astrophys. J. **807**, 151 (2015). arXiv:1503.02315
57. P.A.R. Ade et al., Astrophys. J. **811**, 126 (2015). arXiv:1502.00643
58. BICEP2 Collaboration, Planck Collaboration, P. Ade et al., Phys. Rev. Lett. **114**, 101301 (2015). arXiv:1502.00612